

Inertial Sensor Array Processing with Motion Models

Johan Wahlström^{*}, Isaac Skog[†], Peter Händel[‡]

^{*}Department of Computer Science, University of Oxford, Oxford, UK

[†]Department of Electrical Engineering, Linköping University, Linköping, Sweden

[‡]Department of Information Science and Engineering, KTH Royal Institute of Technology, Stockholm, Sweden

Email: johan.wahlstrom@cs.ox.ac.uk, isaac.skog@liu.se, ph@kth.se

Abstract—By arranging a large number of inertial sensors in an array and fusing their measurements, it is possible to create inertial sensor assemblies with a high performance-to-price ratio. Recently, a maximum likelihood estimator for fusing inertial array measurements collected at a given sampling instance was developed. In this paper, the maximum likelihood estimator is extended by introducing a motion model and deriving a maximum a posteriori estimator that jointly estimates the array dynamics at multiple sampling instances. Simulation examples are used to demonstrate that the proposed sensor fusion method have the potential to yield significant improvements in estimation accuracy. Further, by including the motion model, we resolve the sign ambiguity of gyro-free implementations, and thereby open up for implementations based on accelerometer-only arrays.

I. INTRODUCTION

Thanks to recent advances within micro-electrical-mechanical-system (MEMS) technology, it is now feasible to construct large arrays of inertial sensors also for low-cost applications. In comparison with conventional inertial measurement units (IMUs), inertial arrays offer several benefits [1]. Obviously, the measurement accuracy can be increased by simple averaging. However, since spatially separated accelerometers provide both translational and rotational information (see Fig. 1), it is possible to further reduce the estimation errors by fusing information from accelerometers and gyroscopes¹. Moreover, inertial sensor arrays enable increased dynamic range [2], sensor fault detection and isolation [3], estimation of measurement uncertainties [4], [5], and direct estimation (i.e., not requiring differentiation) of angular acceleration. Recent publications on inertial sensor arrays have focused on sensor calibration [6]–[8], measurement fusion for motion estimation [2], and geometry optimization [9], [10]. There have also been application-specific studies for pedestrian tracking [11], [12], ballistic platform guidance [13], gyro-free navigation [14], biomechanics with safety applications [15], platform stabilization [16], gesture detection [17], and sports performance assessment [18]. Refer to [19] for a survey on inertial sensor arrays.

¹As demonstrated in [2], the angular velocity Fisher information gained from the accelerometers is proportional to the square of the array dimension and to the square of the angular speed.

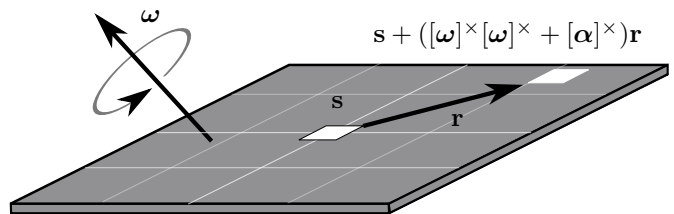


Fig. 1. Spatially separated accelerometers provide both translational and rotational information. The specific force measured by an accelerometer triad at some point \mathbf{r} with respect to the array frame can be expressed as a function of the array’s angular velocity $\boldsymbol{\omega}$, the array’s angular acceleration $\boldsymbol{\alpha}$, and the specific force \mathbf{s} at the origin of the array frame.

Initially, publications on inertial arrays focused on how to extract angular information from different configurations of spatially separated single-axis accelerometers. Typically, the sensor fusion scheme either assumed perfect measurements [20] or relied on a least-squares-based approach [21]. Today, focus has shifted to MEMS applications where the sensors are manufactured in triads and are subject to significant noise. Consequently, [2] derived a maximum likelihood (ML) estimator and the Cramér-Rao bound (CRB) for fusing the measurements from an inertial array with an arbitrary number of accelerometer and gyroscope triads. The model assumed Gaussian measurement noise. Moreover, the proposed estimation method processed measurements from different sampling instances independently, and did not include any motion model that relates the dynamics of the array at one sampling instant to the next.

In this article, the array measurement model is combined with a motion model that couples the angular velocity and angular acceleration at different sampling instances. Consequently, a maximum a posteriori (MAP) estimator is derived to estimate the array’s specific force, angular velocity, and angular acceleration at a sequence of sampling instances. As will be shown, the MAP estimates can be extracted in the same way as the ML estimates. In other words, angular velocity estimates are first computed by numerical means from a concentrated likelihood function. The remaining estimates are then obtained as the solution to a weighted least-squares problem. Further, we discuss identifiability conditions and

derive convenient expressions for the CRB. Last, the accuracy of the estimates are demonstrated in a simulation study. By utilizing information from the motion model, it is possible to both increase the estimation accuracy and improve the identifiability properties. Thanks to the high sampling rate of commercial inertial sensors, motion models can be expected to be of use in a large number of applications, including pedestrian tracking and gesture detection.

II. ESTIMATION

This section describes ML and MAP estimators for the problem of fusing measurements from an inertial sensor array to estimate the array's angular velocity, angular acceleration, and specific force. We begin by reviewing the ML estimator presented in [2]. Following this, we introduce a motion model, and present a MAP estimator that jointly estimates the dynamics at a batch of sampling instances. Last, we discuss how the identifiability properties are affected by the inclusion of the motion model.

A. Model Description

Consider an inertial sensor array with N_a accelerometer triads and N_ω gyroscope triads. The specific force sensed by the n th accelerometer triad is given by [2]

$$\mathbf{s}^{(n)} = \mathbf{s} + ([\boldsymbol{\omega}]^\times [\boldsymbol{\omega}]^\times + [\boldsymbol{\alpha}]^\times) \mathbf{r}^{(n)}. \quad (1)$$

Here, $\mathbf{s}^{(n)}$ and $\mathbf{r}^{(n)}$ denote the specific force and the position in the array frame of the n th accelerometer triad, respectively. Further, \mathbf{s} denotes the specific force at the origin of the array frame. Moreover, $\boldsymbol{\omega}$ and $\boldsymbol{\alpha}$ denote the array's angular velocity and angular acceleration, respectively, and the skew symmetric matrix $[\mathbf{c}]^\times$ is defined so that $[\mathbf{c}_1]^\times \mathbf{c}_2$ is equal to cross product of \mathbf{c}_1 and \mathbf{c}_2 . The measurements from the n th accelerometer triad and the m th gyroscope triad at a given sampling instance are modeled as

$$\tilde{\mathbf{s}}^{(n)} = \mathbf{s}^{(n)} + \boldsymbol{\epsilon}_a^{(n)}, \quad (2a)$$

$$\tilde{\boldsymbol{\omega}}^{(m)} = \boldsymbol{\omega} + \boldsymbol{\epsilon}_\omega^{(m)}, \quad (2b)$$

where $\boldsymbol{\epsilon}_a^{(n)}$ and $\boldsymbol{\epsilon}_\omega^{(m)}$ are measurement noise.

By combining (1) and (2), the measurements $\mathbf{y} \triangleq [(\tilde{\mathbf{s}}^{(1)})^\top \dots (\tilde{\mathbf{s}}^{(N_a)})^\top (\tilde{\boldsymbol{\omega}}^{(1)})^\top \dots (\tilde{\boldsymbol{\omega}}^{(N_\omega)})^\top]^\top$ from the inertial sensor array can be parameterized as [2]

$$\mathbf{y} = \mathbf{h}(\boldsymbol{\omega}) + \mathbf{H}\boldsymbol{\phi} + \boldsymbol{\epsilon} \quad (3)$$

where $\boldsymbol{\epsilon} \triangleq [(\boldsymbol{\epsilon}_a^{(1)})^\top \dots (\boldsymbol{\epsilon}_a^{(N_a)})^\top (\boldsymbol{\epsilon}_\omega^{(1)})^\top \dots (\boldsymbol{\epsilon}_\omega^{(N_\omega)})^\top]^\top$, $\boldsymbol{\phi} \triangleq [\boldsymbol{\alpha}^\top \mathbf{s}^\top]^\top$,

$$\mathbf{h}(\boldsymbol{\omega}) \triangleq \begin{bmatrix} [\boldsymbol{\omega}]^\times [\boldsymbol{\omega}]^\times \mathbf{r}^{(1)} \\ \vdots \\ [\boldsymbol{\omega}]^\times [\boldsymbol{\omega}]^\times \mathbf{r}^{(N_a)} \\ \mathbb{1}_{N_\omega,1} \otimes \boldsymbol{\omega} \end{bmatrix}, \quad \mathbf{H} \triangleq \begin{bmatrix} -[\mathbf{r}^{(1)}]^\times & \mathbf{I}_3 \\ \vdots & \vdots \\ -[\mathbf{r}^{(N_a)}]^\times & \mathbf{I}_3 \\ \mathbf{0}_{3N_\omega,3} & \mathbf{0}_{3N_\omega,3} \end{bmatrix}. \quad (4)$$

Here, $\mathbb{1}_{\ell_1, \ell_2}$, \mathbf{I}_ℓ , $\mathbf{0}_{\ell_1, \ell_2}$, and \otimes denote the matrix of dimension $\ell_1 \times \ell_2$ with all elements equal to one, the identity matrix of dimension ℓ , the zero matrix of dimension $\ell_1 \times \ell_2$, and

the Kronecker product, respectively. Thus, the model can be separated into a nonlinear part $\mathbf{h}(\boldsymbol{\omega})$, that only depends on the angular velocity $\boldsymbol{\omega}$, and a linear part $\mathbf{H}\boldsymbol{\phi}$, that only depends on the angular acceleration $\boldsymbol{\alpha}$ and the specific force \mathbf{s} . Next, we demonstrate how to use this separation to simplify the computation of ML estimates.

B. Maximum Likelihood Estimation

Assuming that the measurement noise $\boldsymbol{\epsilon}$ is a zero-mean Gaussian with covariance \mathbf{R} , the ML estimates of $\boldsymbol{\omega}$, $\boldsymbol{\alpha}$, and \mathbf{s} are given by

$$\begin{aligned} \{\hat{\boldsymbol{\omega}}, \hat{\boldsymbol{\phi}}\} &= \arg \max_{\boldsymbol{\omega}, \boldsymbol{\phi}} p(\mathbf{y} | \boldsymbol{\omega}, \boldsymbol{\phi}) \\ &= \arg \min_{\boldsymbol{\omega}, \boldsymbol{\phi}} \|\mathbf{y} - \mathbf{h}(\boldsymbol{\omega}) - \mathbf{H}\boldsymbol{\phi}\|_{\mathbf{R}^{-1}}^2 \end{aligned} \quad (5)$$

where $\|\mathbf{c}\|_{\mathbf{A}}^2 \triangleq \mathbf{c}^\top \mathbf{A} \mathbf{c}$. Since the model is linear in $\boldsymbol{\phi}$, it is possible to first solve for the optimal $\boldsymbol{\phi}$, as dependent on $\boldsymbol{\omega}$, by means of weighted least-squares. The result can then be substituted back into the likelihood function. This yields a concentrated likelihood function, only dependent on $\boldsymbol{\omega}$, that can be solved by numerical means.

Computationally, the minimization problem is solved in a two-step procedure. In the first step, the angular velocity estimates are computed from

$$\begin{aligned} \hat{\boldsymbol{\omega}} &= \arg \max_{\boldsymbol{\omega}} p(\mathbf{y} | \boldsymbol{\omega}, \hat{\boldsymbol{\phi}}(\boldsymbol{\omega})) \\ &= \arg \min_{\boldsymbol{\omega}} \|\mathbf{y} - \mathbf{h}(\boldsymbol{\omega})\|_{\mathbf{P}}^2 \end{aligned} \quad (6)$$

where

$$\hat{\boldsymbol{\phi}}(\boldsymbol{\omega}) \triangleq (\mathbf{H}^\top \mathbf{R}^{-1} \mathbf{H})^{-1} \mathbf{H}^\top \mathbf{R}^{-1} (\mathbf{y} - \mathbf{h}(\boldsymbol{\omega})) \quad (7)$$

and

$$\mathbf{P} \triangleq \mathbf{R}^{-1} - \mathbf{R}^{-1} \mathbf{H} (\mathbf{H}^\top \mathbf{R}^{-1} \mathbf{H})^{-1} \mathbf{H}^\top \mathbf{R}^{-1}. \quad (8)$$

The optimization problem (6) can be solved by using the Gauss-Newton algorithm [22]. In this case, the estimates are computed by iterating

$$\hat{\boldsymbol{\omega}}^{(i+1)} = \hat{\boldsymbol{\omega}}^{(i)} + (\mathbf{J}^\top \mathbf{P} \mathbf{J})^{-1} \mathbf{J}^\top \mathbf{P} (\mathbf{y} - \mathbf{h}(\hat{\boldsymbol{\omega}}^{(i)})) \quad (9)$$

until convergence. Here, the matrix

$$\mathbf{J} \triangleq \begin{bmatrix} [[\mathbf{r}^{(1)}]^\times \hat{\boldsymbol{\omega}}^{(i)}]^\times - [\hat{\boldsymbol{\omega}}^{(i)}]^\times [\mathbf{r}^{(1)}]^\times \\ \vdots \\ [[\mathbf{r}^{(N_a)}]^\times \hat{\boldsymbol{\omega}}^{(i)}]^\times - [\hat{\boldsymbol{\omega}}^{(i)}]^\times [\mathbf{r}^{(N_a)}]^\times \\ \mathbb{1}_{N_\omega,1} \otimes \mathbf{I}_3 \end{bmatrix} \quad (10)$$

is the Jacobian of $\mathbf{h}(\boldsymbol{\omega})$ evaluated at $\boldsymbol{\omega} = \hat{\boldsymbol{\omega}}^{(i)}$. Once $\hat{\boldsymbol{\omega}}$ has been found, the second step of the procedure extracts the estimates of $\boldsymbol{\phi}$ from (7). Refer to [2] for a discussion on initial estimates $\hat{\boldsymbol{\omega}}^{(0)}$.

C. Maximum a Posteriori Estimation with Motion Prior

In what follows, the estimation procedure presented in [2] will be extended to enable joint estimation of the array dynamics at multiple sampling instances. The notation presented in the previous sections will be augmented with subindices

to denote the relevant sampling instance. Hence, \mathbf{y}_k will for example represent the inertial measurements obtained at sampling instance k . To couple the dynamics at different sampling instances, we introduce the motion model

$$\boldsymbol{\omega}_{k+1} = \boldsymbol{\omega}_k + \Delta t_k \boldsymbol{\alpha}_k + \mathbf{w}_k \quad (11)$$

where \mathbf{w}_k is a noise term, while Δt_k denotes the sampling interval between sampling instances k and $k+1$.

We will now use information from both the measurement model (3) and the motion model (11), while assuming that $\boldsymbol{\epsilon}_k$ and \mathbf{w}_k are mutually independent white Gaussian noise processes with covariances \mathbf{R} and \mathbf{Q} , respectively. The MAP estimates of $\boldsymbol{\omega}_{1:N} \triangleq [\boldsymbol{\omega}_1^\top \dots \boldsymbol{\omega}_N^\top]^\top$ and $\boldsymbol{\phi}_{1:N} \triangleq [\boldsymbol{\phi}_1^\top \dots \boldsymbol{\phi}_N^\top]^\top$, given $\mathbf{y}_{1:N} \triangleq [\mathbf{y}_1^\top \dots \mathbf{y}_N^\top]^\top$, are then

$$\begin{aligned} \{\hat{\boldsymbol{\omega}}_{1:N}, \hat{\boldsymbol{\phi}}_{1:N}\} &= \arg \max_{\boldsymbol{\omega}_{1:N}, \boldsymbol{\phi}_{1:N}} p(\boldsymbol{\omega}_{1:N}, \boldsymbol{\phi}_{1:N} | \mathbf{y}_{1:N}) \\ &= \arg \max_{\boldsymbol{\omega}_{1:N}, \boldsymbol{\phi}_{1:N}} p(\mathbf{y}_{1:N} | \boldsymbol{\omega}_{1:N}, \boldsymbol{\phi}_{1:N}) p(\boldsymbol{\omega}_{1:N}, \boldsymbol{\phi}_{1:N}) \\ &= \arg \max_{\boldsymbol{\omega}_{1:N}, \boldsymbol{\phi}_{1:N}} \prod_{k=1}^N p(\mathbf{y}_k | \boldsymbol{\omega}_k, \boldsymbol{\phi}_k) \quad (12) \\ &\quad \cdot \prod_{k=1}^{N-1} p(\boldsymbol{\omega}_{k+1} | \boldsymbol{\omega}_k, \boldsymbol{\alpha}_k) \\ &= \arg \min_{\boldsymbol{\omega}_{1:N}, \boldsymbol{\phi}_{1:N}} \sum_{k=1}^N \|\mathbf{y}_k - \mathbf{h}(\boldsymbol{\omega}_k) - \mathbf{H}\boldsymbol{\phi}_k\|_{\mathbf{R}^{-1}}^2 \\ &\quad + \sum_{k=1}^{N-1} \|\boldsymbol{\omega}_{k+1} - \boldsymbol{\omega}_k - \Delta t_k \boldsymbol{\alpha}_k\|_{\mathbf{Q}^{-1}}^2 \\ &= \arg \min_{\boldsymbol{\omega}_{1:N}, \boldsymbol{\phi}_{1:N}} \|\bar{\mathbf{y}} - \bar{\mathbf{h}}(\boldsymbol{\omega}_{1:N}) - \bar{\mathbf{H}}\boldsymbol{\phi}_{1:N}\|_{\bar{\mathbf{R}}^{-1}}^2 \end{aligned}$$

where we have used the uninformative priors $p(\boldsymbol{\omega}_1) \propto 1$ and $p(\boldsymbol{\alpha}_1) \propto 1$. Hence, no assumption is made on the initial dynamics. Further, we have defined $\bar{\mathbf{y}} \triangleq [\mathbf{y}_{1:N}^\top \mathbf{0}_{1,3(N-1)}]^\top$, $\bar{\mathbf{R}} \triangleq \text{blkdiag}(\mathbf{I}_N \otimes \mathbf{R}, \mathbf{I}_{N-1} \otimes \mathbf{Q})$,

$$\bar{\mathbf{h}}(\boldsymbol{\omega}_{1:N}) \triangleq \begin{bmatrix} \mathbf{h}(\boldsymbol{\omega}_1) \\ \vdots \\ \mathbf{h}(\boldsymbol{\omega}_N) \\ \boldsymbol{\omega}_1 - \boldsymbol{\omega}_2 \\ \vdots \\ \boldsymbol{\omega}_{N-1} - \boldsymbol{\omega}_N \end{bmatrix}, \quad \bar{\mathbf{H}} \triangleq \begin{bmatrix} \mathbf{I}_N \otimes \mathbf{H} \\ \mathbf{H}' & \mathbf{0}_{3(N-1),6} \end{bmatrix}, \quad (13)$$

$\mathbf{H}' \triangleq \mathbf{H}'_1 \oplus \dots \oplus \mathbf{H}'_{N-1}$, and $\mathbf{H}'_k \triangleq [\Delta t_k \mathbf{I}_3 \mathbf{0}_3]$. Here, $\text{blkdiag}(\cdot, \dots, \cdot)$ and \oplus denote a block diagonal matrix with block matrices given by the arguments and the direct sum of two matrices, respectively. Since (12) is on the same form as (5), it can be solved using the same approach as in Section II-B. Thus, we would first use the Gauss-Newton algorithm to obtain $\hat{\boldsymbol{\omega}}_{1:N}$. Here, the Jacobian of $\bar{\mathbf{h}}(\boldsymbol{\omega}_{1:N})$ evaluated at $\boldsymbol{\omega}_{1:N} = \hat{\boldsymbol{\omega}}_{1:N}^{(i)}$ is $\bar{\mathbf{J}} \triangleq [(\mathbf{J}^a)^\top (\mathbf{J}^b)^\top]^\top$, where $\mathbf{J}^a \triangleq \mathbf{J}(\hat{\boldsymbol{\omega}}_1^{(i)}) \oplus \dots \oplus \mathbf{J}(\hat{\boldsymbol{\omega}}_N^{(i)})$ and $\mathbf{J}^b \triangleq [\mathbf{I}_{3(N-1)} \mathbf{0}_{3(N-1),3}] - [\mathbf{0}_{3(N-1),3} \mathbf{I}_{3(N-1)}]$. The initial estimate of $\boldsymbol{\omega}$ can be obtained by using the initial estimates proposed in [2] at each sampling instance. In the second step, $\hat{\boldsymbol{\omega}}_{1:N}$ is used to obtain an estimate of $\boldsymbol{\phi}_{1:N}$. As a last observation, note that the motion models $\boldsymbol{\alpha}_{k+1} = \boldsymbol{\alpha}_k + \mathbf{w}_{\alpha,k}$ and $\mathbf{s}_{k+1} = \mathbf{s}_k + \mathbf{w}_{a,k}$, where $\mathbf{w}_{\alpha,k}$ and $\mathbf{w}_{a,k}$ are white Gaussian noise processes, can be incorporated into the estimation in the same manner as the model (11).

D. Identifiability Conditions

The identifiability conditions for the model (3) have previously been discussed in [2]. Specifically, it was concluded that necessary and sufficient conditions for the parameters $\boldsymbol{\omega}$, $\boldsymbol{\alpha}$, and \mathbf{s} to be identifiable are that the array has i) at least one gyroscope triad; and ii) at least three accelerometer triads whose locations span a two-dimensional space. By including the motion model (11), the sign ambiguity of $\boldsymbol{\omega}$ when excluding the gyroscope measurements is resolved (note that we may have $\bar{\mathbf{h}}(\boldsymbol{\omega}_{1:N}) \neq \bar{\mathbf{h}}(-\boldsymbol{\omega}_{1:N})$ also when $N_\omega = 0$). Thus, in this case, only condition ii) remains².

III. THE CRAMÉR-RAO BOUND

A common way to assess the performance of an estimator is to compare its mean square error to the CRB. Assuming that all errors are Gaussians, it is straightforward to derive the Bayesian CRB for $\boldsymbol{\theta} \triangleq [\boldsymbol{\omega}_{1:N}^\top \boldsymbol{\phi}_{1:N}^\top]^\top$ as

$$\text{Cov}(\boldsymbol{\theta}) \succeq \mathcal{I}_B(\boldsymbol{\theta})^{-1} \quad (14)$$

where it holds that [24]

$$\mathcal{I}_B(\boldsymbol{\theta}) = \boldsymbol{\Phi}^\top \bar{\mathbf{R}}^{-1} \boldsymbol{\Phi} \quad (15)$$

and the linearized measurement matrix is given by $\boldsymbol{\Phi} \triangleq [\bar{\mathbf{J}} \bar{\mathbf{H}}]$. Here, we have used $\mathbf{A} \succeq \mathbf{B}$ to denote that $\mathbf{A} - \mathbf{B}$ is positive semidefinite. Alternatively, $\mathcal{I}_B(\boldsymbol{\theta})$ can be decomposed as

$$\mathcal{I}_B(\boldsymbol{\theta}) = \mathcal{I}_D(\boldsymbol{\theta}) + \mathcal{I}_P(\boldsymbol{\theta}) \quad (16)$$

where $\mathcal{I}_D(\boldsymbol{\theta})$ and $\mathcal{I}_P(\boldsymbol{\theta})$ represent the information gained from the observed data and from the motion prior, respectively. Specifically, if we reorder the parameters as $\boldsymbol{\theta} \triangleq [\boldsymbol{\theta}_1^\top \dots \boldsymbol{\theta}_N^\top]^\top$, where $\boldsymbol{\theta}_k \triangleq [\boldsymbol{\omega}_k^\top \boldsymbol{\phi}_k^\top]^\top$, it holds that

$$\mathcal{I}_D(\boldsymbol{\theta}) = \text{blkdiag}(\mathcal{I}(\boldsymbol{\theta}_1), \dots, \mathcal{I}(\boldsymbol{\theta}_N)) \quad (17)$$

where $\mathcal{I}(\boldsymbol{\theta}_k)$ is the Fisher information matrix (FIM) for estimating $\boldsymbol{\theta}_k$ without any motion prior. Expressions for $\mathcal{I}(\boldsymbol{\theta}_k)$ have previously been presented in [2]. Further, assuming a constant sampling interval $\Delta t_k = \Delta t$, it holds that

$$\begin{aligned} \mathcal{I}_P(\boldsymbol{\theta}) &= \mathbf{D}_1 \otimes \mathbf{T}_1 + \mathbf{D}_2 \otimes \mathbf{T}_2 \\ &\quad + (\mathbf{D}_3 \otimes \mathbf{T}_3) + \mathbf{D}_3^\top \otimes \mathbf{T}_3^\top \end{aligned} \quad (18)$$

where

$$\mathbf{D}_1 = \begin{bmatrix} 1 & 0 & \dots & \dots & 0 \\ 0 & 2 & \ddots & & \vdots \\ \vdots & \ddots & \ddots & \ddots & \vdots \\ \vdots & & \ddots & 2 & 0 \\ 0 & \dots & \dots & 0 & 1 \end{bmatrix}, \quad \mathbf{D}_2 = \begin{bmatrix} 1 & 0 & \dots & \dots & 0 \\ 0 & 1 & \ddots & & \vdots \\ \vdots & \ddots & \ddots & \ddots & \vdots \\ \vdots & & \ddots & 1 & 0 \\ 0 & \dots & \dots & 0 & 0 \end{bmatrix}, \quad (19)$$

²Although the idea of using a motion model to facilitate the fusion of measurements from gyro-free arrays is not new [23], this is the first time that it is used as an extension of the estimation formulation described in [2].

and

$$\mathbf{D}_3 = \begin{bmatrix} 0 & -1 & \cdots & \cdots & 0 \\ 0 & 0 & \ddots & & \vdots \\ \vdots & \ddots & \ddots & \ddots & \vdots \\ \vdots & & \ddots & 0 & -1 \\ 0 & \cdots & \cdots & 0 & 0 \end{bmatrix} \quad (20)$$

are all matrices of dimension $N \times N$. Further, we have $\mathbf{T}_1 \triangleq \text{blkdiag}(\mathbf{Q}^{-1}, \mathbf{0}_{6,6})$,

$$\mathbf{T}_2 \triangleq \begin{bmatrix} 0 & \Delta t & 0 \\ \Delta t & (\Delta t)^2 & 0 \\ 0 & 0 & 0 \end{bmatrix} \otimes \mathbf{Q}^{-1}, \quad (21)$$

and

$$\mathbf{T}_3 \triangleq \begin{bmatrix} 1 & 0 & 0 \\ \Delta t & 0 & 0 \\ 0 & 0 & 0 \end{bmatrix} \otimes \mathbf{Q}^{-1}. \quad (22)$$

Obviously, the motion model (11) provides more information in applications where the elements of \mathbf{Q} are small, i.e., when the sampling rate is high and the array dynamics are low.

To interpret the different terms in (18), consider the formulation where the CRB is the expectation of a Hessian matrix [22], [24]. In this case, the term $\mathbf{D}_1 \otimes \mathbf{T}_1$ reflects second-order derivatives with respect to ω_k . Similarly, $\mathbf{D}_2 \otimes \mathbf{T}_2$ is associated with mixed partial derivatives with respect to ω_k and α_k , and second-order derivatives with respect to α_k , while $\mathbf{D}_3 \otimes \mathbf{T}_3$ reflects mixed partial derivatives with respect to ω_k and ω_{k+1} , and with respect to α_k and ω_{k+1} .

IV. SIMULATIONS

Next, simulations are used to compare the MAP estimator in Section II-C to the ML estimator discussed in Section II-B and the CRBs from Section III. We also illustrate estimation using gyro-free arrays. The examples are inspired by the simulations presented in [2].

A. Setup

Measurements were simulated from four gyroscope triads and four accelerometer triads located at $\mathbf{r}^{(1)} = 0.01 \cdot [1 \ 0 \ 0]^T [m]$, $\mathbf{r}^{(2)} = 0.01 \cdot [-1 \ 0 \ 0]^T [m]$, $\mathbf{r}^{(3)} = 0.01 \cdot [0 \ 1 \ 0]^T [m]$, and $\mathbf{r}^{(4)} = 0.01 \cdot [0 \ -1 \ 0]^T [m]$. The sensor geometry is illustrated in Fig. 2. Temporally and mutually uncorrelated measurement errors were simulated with standard deviations of $\sigma_a = 0.01 [m/s^2]$ and $\sigma_\omega = 1 [^\circ/s]$ in each spatial direction (refer to [2] for a discussion on sensor noise variances).

Once the angular velocity had been specified (see Sections IV-B, IV-C, and IV-D), the angular acceleration was simulated as $\alpha_k = (\omega_{k+1} - \omega_k - \mathbf{w}_k)/\Delta t$. Here, we set $\Delta t = 0.05 [s]$ and $\mathbf{Q} = \sigma_q^2 \mathbf{I}_3$ with $\sigma_q = 0.01 \cdot 180/\pi [^\circ/s]$. Hence, $\mathbf{w}_k/\Delta t$ had a standard deviation of about $10 [^\circ/s]$. The orientation of the array was defined by letting the initial orientation matrix be the identity matrix and then iteratively updating the orientation matrix based on the specified angular velocities. The acceleration at the origin of the array was initialized as $\mathbf{a}_1 = \mathbf{0}_{3,1}$, and was then iteratively updated according to

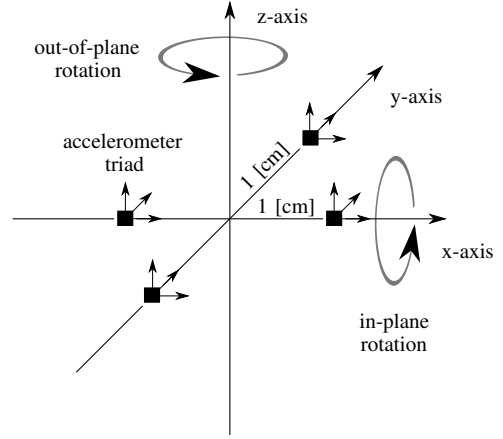


Fig. 2. Sensor geometry in the simulations.

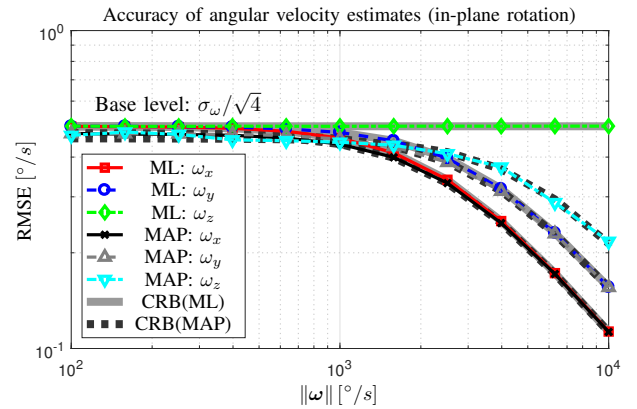


Fig. 3. Comparison of ML and MAP estimators.

$\mathbf{a}_{k+1} = \mathbf{a}_k + \mathbf{w}_k^{(v)}$. Here, $\mathbf{w}_k^{(v)}$ was assumed to be a white Gaussian noise process with covariance $\sigma_a^2 \mathbf{I}_3$, where $\sigma_a = 0.2 [m/s^2]$. Finally, the specific force at the accelerometer positions was computed by adding the gravitational component (based on the array orientation³) and the centrifugal force and the Euler force (based on (1) and the array's angular dynamics and sensor geometry). The root-mean-square errors (RMSEs) were computed by applying the estimators to 10^6 different data realizations.

B. Example 1 — In-plane Rotation

In the first example, we consider rotations around the x-axis, so that $\omega_k = 10^{1.6+0.2 \cdot k} \cdot [1 \ 0 \ 0]^T [^\circ/s]$ for $k = 1, \dots, 13$. Fig. 6 illustrates the RMSEs of the MAP estimator and the ML estimator (which processed the measurements from each sampling instance independently)⁴. At high angular speeds, the MAP estimator can be seen to provide substantially better estimates of the angular velocity in the z-direction. In this example, the ML estimator gains no information from the accelerometers

³The specific force at the origin of the array frame is $\mathbf{s} = \mathbf{a} - \mathbf{g}$, where \mathbf{g} denotes the gravity force in the array frame.

⁴To ensure that the choice of sampling boundary does not have an impact on the displayed accuracy (see e.g., the information provided by the term $\mathbf{D}_1 \otimes \mathbf{T}_1$ in (18)), Fig. 6 only shows the RMSEs for $\omega_2, \dots, \omega_{N-1}$.

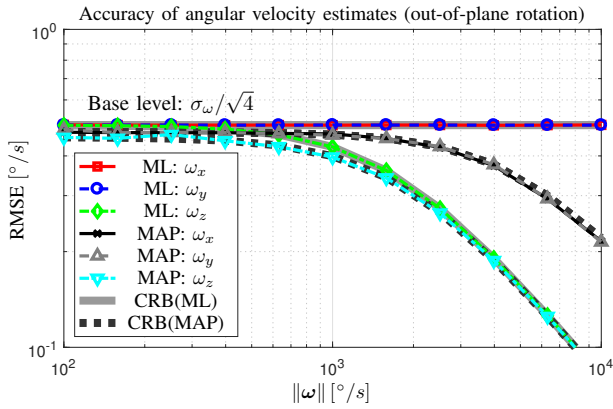


Fig. 4. Comparison of ML and MAP estimators.

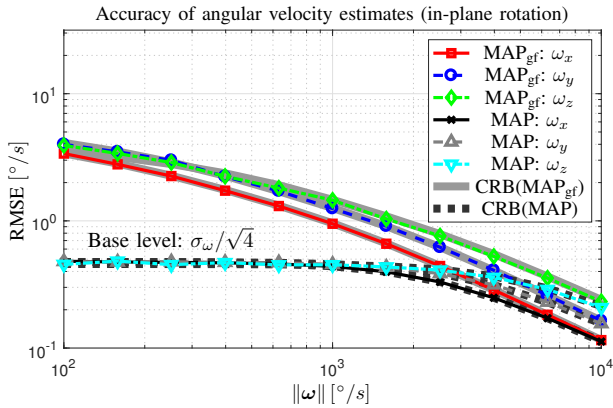


Fig. 5. Comparison with gyro-free array.

about the angular velocity in the z-direction [2]. Thus, the corresponding RMSE is equal to the base level that is reached by simply averaging the gyroscope measurements. However, by including the motion model, additional information is gained about the angular velocity at high angular speeds. Both the MAP and the ML estimator achieve their respective CRBs (with and without information from the motion model). The MAP and ML estimators provide similar RMSEs along the x and y-axes.

C. Example 2 — Out-of-plane Rotation

Here, we used $\omega_k = 10^{1.6+0.2 \cdot k} \cdot [0 \ 0 \ 1] [^\circ/s]$ for $k = 1, \dots, 13$. While Fig. 5 shows that the ML estimates are at the base level along the x and y-axes, the MAP estimator clearly displays better performance at high angular speeds. Once again, both estimators achieve their respective CRBs. To summarize, examples 1 and 2 illustrate that in the general case with rotations along all axes, the MAP estimator can be expected to provide enhanced angular velocity estimates along all axes.

D. Example 3 — Gyro-free Arrays

The dynamics from example 1 were reused to demonstrate how the motion model enables parameter estimation using gyro-free arrays. Fig. 5 compares the MAP estimator from example 1 with the corresponding gyro-free MAP estimator,

denoted by MAP_{gf} . As expected, the two estimators display practically equivalent RMSEs at high angular speeds.

V. CONCLUSIONS

This paper has presented a MAP estimator for estimating the angular velocity, angular acceleration, and specific force of an inertial sensor array. The estimator does not only use information from a measurement model, but also incorporates a motion model which e.g., enables identifiability of all parameters also in cases when no gyroscopes are available. Through simulations, it was found that the estimator achieves the Cramér-Rao bound and yields a substantial performance gain in comparison to when no motion model is used.

ACKNOWLEDGEMENTS

This research has financially supported by the Swedish Foundation for Strategic Research (SSF) via the project *AS-SEMBLE*.

REFERENCES

- [1] I. Skog, J. O. Nilsson, and P. Händel, "An open-source multi inertial measurement unit (MIMU) platform," in *Int. Symp. Inertial Sensors Syst.*, Laguna Beach, CA, Feb. 2014.
- [2] I. Skog, J. O. Nilsson, P. Händel, and A. Nehorai, "Inertial sensor arrays, maximum likelihood, and Cramér-Rao bound," *IEEE Trans. Signal Process.*, vol. 64, no. 16, pp. 4218–4227, Aug. 2016.
- [3] S. Sukkarieh, P. Gibbens, B. Grocholsky, K. Willis, and H. F. Durrant-Whyte, "A low-cost, redundant inertial measurement unit for unmanned air vehicles," *Int. J. Robot. Research*, vol. 19, no. 11, pp. 1089–1103, Nov. 2000.
- [4] A. Waegli, J. Skaloud, S. Guerrier, M. E. Parés, and I. Colomina, "Noise reduction and estimation in multiple micro-electro-mechanical inertial systems," *Meas. Sci. Technol.*, vol. 21, no. 6, Apr. 2010.
- [5] M. Schwaab, S. A. Reginya, A. Sikora, and E. V. Abramov, "Measurement analysis of multiple MEMS sensor array," in *IEEE Int. Conf. Integr. Navigation Syst.*, Saint Petersburg, Russia, May 2017.
- [6] J. O. Nilsson, I. Skog, and P. Händel, "Aligning the forces — Eliminating the misalignments in IMU arrays," *IEEE Trans. Instrum. Meas.*, vol. 63, no. 10, pp. 2498–2500, Oct. 2014.
- [7] J. Wahlström, I. Skog, P. Händel, and A. Nehorai, "IMU-based smartphone-to-vehicle positioning," *IEEE Trans. Intell. Vehicles*, vol. 1, no. 2, pp. 139–147, Jul. 2016.
- [8] H. Carlsson, I. Skog, and J. Jaldén, "On-the-fly geometric calibration of inertial sensor arrays," in *IEEE Int. Conf. Indoor Positioning and Indoor Navigation*, Sapporo, Japan, Sep. 2017.
- [9] R. Hanson and M. Pachter, "Optimal gyro-free IMU geometry," in *AIAA Int. Conf. Guidance, Navigation, and Control*, San Francisco, CA, Aug. 2005.
- [10] S. Bose, A. K. Gupta, and P. Handel, "On the noise and power performance of a shoe-mounted multi-imu inertial positioning system," in *IEEE Int. Conf. Indoor Positioning and Indoor Navigation*, Sapporo, Japan, Sep. 2017.
- [11] I. Skog, J. O. Nilsson, and P. Händel, "Pedestrian tracking using an IMU array," in *IEEE Int. Conf. Electron., Comput. Commun. Technol.*, Bangalore, India, Jan. 2014.
- [12] C. Tjhai and K. O'Keefe, "Step-size estimation using fusion of multiple wearable inertial sensors," in *IEEE Int. Conf. Indoor Positioning and Indoor Navigation*, Sapporo, Japan, Sep. 2017.
- [13] M. Costello and T. Jitpraphai, "Determining angular velocity and angular acceleration of projectiles using triaxial acceleration measurements," *J. Spacecraft and Rockets*, vol. 39, no. 1, pp. 73–80, Jan. 2002.
- [14] M. Pachter, T. C. Welker, and R. E. Huffman, "Gyro-free INS theory," *Navigation*, vol. 60, no. 2, pp. 85–96, Jun. 2013.
- [15] D. B. Camarillo, P. B. Shull, J. Mattson, R. Shultz, and D. Garza, "An instrumented mouthguard for measuring linear and angular head impact kinematics in American football," *Ann. Biomed. Eng.*, vol. 41, no. 9, pp. 1939–1949, Sep. 2013.

- [16] M. C. Algrain and J. Quinn, "Accelerometer based line-of-sight stabilization approach for pointing and tracking systems," in *Proc. IEEE Int. Conf. Control Appl.*, Vancouver, BC, Sep. 1993, pp. 159–163.
- [17] X. Wang and C. Yang, "Constructing gyro-free inertial measurement unit from dual accelerometers for gesture detection," *Sensors & Transducers J.*, vol. 171, no. 5, pp. 134–140, May 2014.
- [18] A. Waegli, S. Guerrier, and J. Skaloud, "Redundant MEMS-IMU integrated with GPS for performance assessment in sports," in *IEEE/ION Position, Location and Navigation Symp.*, Monterey, CA, May 2008, pp. 1260–1268.
- [19] J. O. Nilsson and I. Skog, "Inertial sensor arrays — A literature review," in *European Navigation Conf.*, Helsinki, Finland, May 2016.
- [20] A. R. Schuler, A. Grammatikos, and K. A. Fegley, "Measuring rotational motion with linear accelerometers," *IEEE Trans. Aerosp. Electron. Syst.*, vol. AES-3, no. 3, pp. 465–472, May 1967.
- [21] J. Angeles, "Computation of rigid-body angular acceleration from point-acceleration measurements," *J. Dyn. Sys., Meas., Control*, vol. 109, no. 2, pp. 124–127, Jun. 1987.
- [22] S. M. Kay, *Fundamentals of Statistical Signal Processing: Estimation Theory*. Prentice-Hall, 1993.
- [23] T. R. Williams, D. W. Raboud, and K. R. Fyfe, "Minimal spatial accelerometer configurations," *J. Dyn. Sys., Meas., Control*, vol. 135, no. 2, Feb. 2013.
- [24] H. L. Van Trees, *Detection, Estimation, and Modulation Theory: Part I*. Wiley, 1968.